

# MIKA - a multigrid-based program package for electronic structure calculations

T. Torsti<sup>1,2</sup>, V. Lindberg<sup>3</sup>, I. Makkonen<sup>1</sup>, E. Ogando<sup>4</sup>,  
E. Räsänen<sup>1</sup>, H. Saarikoski<sup>1</sup>, M. J. Puska<sup>1</sup> and R. M. Nieminen<sup>1</sup>

<sup>1</sup>*Laboratory of Physics, Helsinki University of Technology,  
P.O. Box 1100, FIN-02015 HUT, Finland,*

<sup>2</sup>*CSC – Scientific Computing Ltd., P.O. Box 405, FIN-20101 Espoo, Finland,*

<sup>3</sup>*Department of Physics, Växjö University, SE-351 95 Växjö, Sweden,*

<sup>4</sup>*Donostia International Physics Center (DIPC),  
1072 Posta Kutxa, 20080 Donostia, Spain*

### Abstract

We give an introduction to the real-space, multigrid-based program package MIKA (Multigrid Instead of the K-spAce). We give a short account of the history of real-space methods, introduce the idea of multigrid acceleration techniques, and present a generalisation of the Rayleigh-quotient minimization multigrid method. We also describe recent technical improvements of the numerical methods, and give examples of the most recent applications of the program package. The software developed in the MIKA-project is freely available in the hope that it will be useful for the researchers in the electronic structure community in general.

## 1 Introduction

In this article, we give an overview of the real-space, multigrid-based program package called MIKA. It consists of several different modules for solving the Kohn-Sham equations of the density-functional theory in different geometries. The program package is visualized in Fig. 1. It is emphasized in this figure that all the four application codes `rspace`, `cy12`, `doppler` and `rs2dot` share common numerical multigrid routines implemented in the subroutine library `MGLIB`. This,

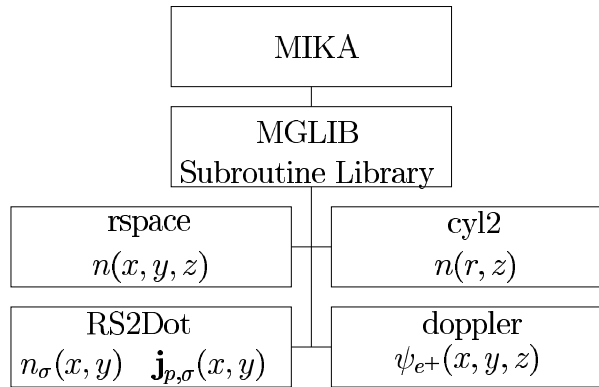


Figure 1: Schematic illustration of the software comprising the MIKA-package. Each of the four applications comes with a version of the numerical multigrid subroutine library MGLIB. Examples of applications of each of these codes are given in the text.

however, is in practice not true. There is a common ancestor to the multigrid subroutines, but in practice each code comes with its own version of the subroutine library. Some version of each of the codes is available from the MIKA-webpage [1]. The full source code is available, and the source code is licensed with the GNU general public license (GPL)<sup>1</sup>. Therefore, it is fully acceptable, and even recommended, for other researchers to take a piece of software that he/she considers useful, make further improvements, and start distributing the derived product on his/her own web-page. We believe that such a distributed mode of development, based on voluntary work of researchers, should in the long run be more efficient than a centralized mode. Of course, some form of centralized effort may be necessary to coordinate such activity.

The outline of this article is as follows. In section 2 we give, for the sake of completeness, the Kohn-Sham equations, the numerical solution of which is the subject of the rest of this article. In section 3 we give first some motivation for using grid-based real-space methods as opposed to plane-wave schemes and techniques based on the use of atom-centered basis functions. We use the standard and well-known multigrid solver for the Poisson equation to illustrate the basic ideas of the multigrid methodology. We then give a classification of three different types of multigrid techniques appearing in the literature for the eigenvalue problem. Without making any conclusions about the relative efficiency of the three approaches, we proceed to describe in detail our own approach, the Rayleigh-quotient minimization multigrid (RQMG) method [5]. In section 4 we outline various technical improvements related to the RQMG method, to efficient methods for reaching self consistency, and to the computationally inexpensive use of auxiliary finer grids to improve the numerical accuracy of real-space grid-based calculations in general. Sections 5-8 contain brief introductions to the applications of our MIKA-package in general three-dimensional pseudopotential calculations for both finite and periodic systems, quantum dots in two-dimensional electron gas, axially symmetric jellium models for nanostructures and for the calculation of positron states in solids, respectively. In addition to these, a modification of the RQMG method for one-dimensional problems has been applied by Ogando et al. to treat thin metallic films on solid surfaces [6, 7].

<sup>1</sup>This seems to be a general trend in our community, advocated by the `fsatom` project [2], and followed e.g. by the `abinit` [3] and `octopus` [4] -projects.

## 2 Formalism

In the Kohn-Sham method for electronic structure calculations one solves for a set of equations self-consistently [8]. In the following, for the sake of completeness and simplicity, we present the equations and do so in the spin-compensated form, respectively. In practice, where needed (i.e. thus far for the `rs2dot` and `cy12` -codes), we have made the straightforward generalization using the spin-density functional theory. The set of equations reads as (atomic units with  $\hbar = m_e = e = 1$  are used):

$$\left(-\frac{1}{2}\nabla^2 + V_{\text{eff}}(\mathbf{r})\right)\Psi_i = \epsilon_i\Psi_i, \quad (1)$$

$$n(\mathbf{r}) = \sum_i^N |\Psi_i(\mathbf{r})|^2, \quad (2)$$

$$V_{\text{eff}}(\mathbf{r}) = V_{\text{ion}}(\mathbf{r}) + V_{\text{H}}(\mathbf{r}) + V_{\text{xc}}(\mathbf{r}), \quad (3)$$

$$V_{\text{H}}(\mathbf{r}) = \int \frac{n(\mathbf{r}')}{|\mathbf{r} - \mathbf{r}'|} d\mathbf{r}', \quad (4)$$

$$V_{\text{xc}}(\mathbf{r}) = \frac{\delta E_{\text{xc}}[n(\mathbf{r})]}{\delta n(\mathbf{r})}. \quad (5)$$

The first equation (1) is a Schrödinger equation for non-interacting particles in an effective potential  $V_{\text{eff}}(\mathbf{r})$ . For finite systems the wave functions are required to vanish at the boundaries of the computation volume. In the case of infinite periodic systems the complex wave functions have to obey the Bloch theorem at the cell boundaries. The electron density  $n(\mathbf{r})$  is obtained from a sum over the  $N$  occupied states. The effective potential consists of an external potential  $V_{\text{ion}}(\mathbf{r})$  due to ions (or nuclei in all-electron calculations), the Hartree potential  $V_{\text{H}}(\mathbf{r})$  calculated from the electron density distribution, and the exchange-correlation potential  $V_{\text{xc}}(\mathbf{r})$ . In the examples of the present article we use the local-density approximation (LDA) for the exchange-correlation energy

$$E_{\text{xc}}[n(\mathbf{r})] = \int \epsilon_{\text{xc}}(n(\mathbf{r}))n(\mathbf{r})d\mathbf{r}, \quad (6)$$

and for the exchange-correlation potential

$$V_{\text{xc}}(\mathbf{r}) = \epsilon_{\text{xc}}(n(\mathbf{r})) + n(\mathbf{r}) \left. \frac{d\epsilon_{\text{xc}}}{dn} \right|_{n=n(\mathbf{r})}. \quad (7)$$

The Hartree potential is solved from the Poisson equation

$$\nabla^2 V_{\text{H}}(\mathbf{r}) = -4\pi n(\mathbf{r}). \quad (8)$$

In practice, the electron density  $n(\mathbf{r})$  is substituted by the total charge density  $\rho(\mathbf{r})$ , which includes a positive charge neutralizing the system. This positive charge is composed of Gaussian charge (with charge  $Z_I$ ) distributions centered at the ions  $I$ . Once Eq. 8 is numerically solved, the analytically known potential caused by the Gaussians is replaced by the local part of the pseudopotential. Obviously, this correction has finite range, since both potentials have the asymptotic behaviour  $Z_I/|\mathbf{r} - \mathbf{r}_I|$ . In the case of finite systems, Dirichlet boundary conditions are used with the Coulomb potential values calculated using a multipole expansion. For periodic systems we fix the average Coulomb potential to zero – this is equivalent to setting  $V_C(G =$

0) = 0 in the plane-wave approach – and allow the periodic boundary conditions to result in the corresponding converged potential.

The self-consistent solution of the above Kohn-Sham equations leads to the ground state electronic structure minimizing the total energy

$$\begin{aligned}
 E_{\text{tot}} = & \sum_i \int \Psi_i^*(\mathbf{r}) \left( -\frac{1}{2} \nabla^2 \right) \Psi_i(\mathbf{r}) d\mathbf{r} + \frac{1}{2} \int V_{\text{H}}(\mathbf{r}) n(\mathbf{r}) d\mathbf{r} \\
 & + \int V_{\text{ion}}(\mathbf{r}) n(\mathbf{r}) d\mathbf{r} + E_{\text{xc}} + E_{\text{ion-ion}} ,
 \end{aligned} \tag{9}$$

where  $E_{\text{ion-ion}}$  is the repulsive interaction between the ions (nuclei) of the system. Instead of the self-consistency iterations the solution of the Kohn-Sham problem can be found by minimizing directly the total energy with respect to the wave function parameters, *e.g.* plane-wave coefficients [9]. However, Kresse and Furthmüller [10, 11] have found this scheme less efficient than the self-consistency iterations.

### 3 Real-space (multigrid) methods

The plane-wave pseudopotential method has proven to be an excellent computational tool for solving large-scale electronic structure problems in condensed matter physics [12, 9]. Notable strengths of the method are the ability to use the fast Fourier transform for updating the Kohn-Sham equations, lack of dependence of the basis on atom positions, and the clear control of convergence with the cutoff energy determined by the shortest-wavelength mode. However, the method encounters difficulties in treating widely varying length scales. This issue is relevant for all-electron calculations, surfaces, clusters, and the hard pseudopotentials of first-row elements or transition metals. It is not necessary to use the supercell approximation, when treating clusters or molecules with real-space methods. However, it should be noted that this is not necessary in the plane-wave methodology either [13].

Approaches, where the basis functions are atom-centered or floating Gaussians or atomic orbitals, are very well established, and are used by the majority of the quantum-chemistry community as well as by an increasing number of condensed-matter physicists. A wide selection of well-established codes based on atom-centered basis functions is available, including *e.g.* DMOL [14], ADF [15], TURBOMOLE [16], NWCHEM [17] and SIESTA [18], among others. The basis sets used in these methods are at least an order of magnitude smaller than in the plane-wave methods, but the magnitude of the related basis-set truncation error is difficult to estimate.

Considerable effort has recently been focused also on developing “fully numerical” real-space methods [19], which permit systematic studies of convergence in the spirit of the plane-wave methods. These methods are based on finite elements [20, 21, 22, 23, 24], finite-difference discretizations [25, 26, 27, 28, 29, 30, 31] or wavelets [32]. Advantages of these approaches include the free choice of boundary conditions, allowing *e.g.* the treatment of finite and periodic systems with equal effort. Near-locality of the kinetic energy operator in real-space representations leads to simplicity in developing domain-decomposition parallel algorithms. In addition, it is possible to implement adaptive grid-refinement strategies to focus effort in spatial regions with large variations in the computed functions, for example near the nuclei. In finite-difference methods,

the available strategies for mesh refinement include composite grids [33, 34, 35] and adaptive coordinates [36, 31]. In finite-element methods, on the other hand, there is in principle complete freedom in the choice of the computational mesh. However, generating an optimal finite element mesh (or finite-difference composite grid) for a given problem is a nontrivial task [37, 38, 39], which either requires *a priori* knowledge of the spatial dependence of the required density of the mesh, or involves a repeated sequence of solving the problem in a given mesh, making an *a posteriori* error estimation and then remeshing. Representations on real space grids allow also the use of multigrid (MG) algorithms with their excellent convergence characteristics and scaling properties [40, 41]. A real-space formulation is also often used in efficient implementations of  $O(N)$  electronic structure methods, in which the computational work required scales linearly with the number of atoms [42, 43].

Among the pioneers of real-space methods for molecular systems were A. D. Becke [44, 45] and Pyykkö *et al.* [46, 47, 48], who made highly accurate fully numerical all-electron real-space calculations for diatomic molecules, employing the prolate spheroidal coordinate system. In the axial symmetry of diatomic molecules, the azimuthal dependence of the single-particle functions can be treated analytically and the ensuing numerical problem is two-dimensional. Their approach for diatomic molecules is very similar to our more general method for axially symmetric systems, described in Sec. 7. Besides the density-functional theory, Pyykkö *et al.* applied their fully numerical approach to other quantum chemical models such as Hartree-Fock, MCSCF, and Relativistic DFT [46].

Several approaches employing the multigrid idea within electronic structure calculations have appeared during the last decade [5, 49, 27, 28, 43, 30, 29]. The main idea of multigrid methods is that they avoid the critical slowing-down (CSD) phenomenon occurring when a partial differential equation discretized on a real space grid is solved with a simple relaxation method such as the Gauss-Seidel method. The discretized operators use information from a rather localized region of the grid at a time. Therefore the high-frequency error of the length scale of the grid spacing is reduced very rapidly in the relaxation. However, once the high-frequency error has effectively been removed, the slow convergence of the low-frequency components dominates the overall error reduction rate [40], i.e. CSD occurs. In multigrid methods one stops the relaxation on a given (fine) grid before CSD sets in and transfers the equation to a coarser grid (the so-called *restriction* operation) where the low-frequency components can be solved more efficiently. On the coarsest grid the problem is solved exactly or as accurately as possible, after which one interpolates (the so-called *prolongation* operation) the correction to finer grids, performing simultaneously relaxations in order to remove the high-frequency errors introduced in the interpolation.

It is best to illustrate these ideas in the case of the simple Poisson problem  $\nabla^2 V = f$ . After a few relaxation sweeps on the fine grid  $f$  the rapidly varying components of the residual  $R_f = f - \nabla^2 V_f$  have been efficiently damped. A smooth correction  $V_c$  (approximately satisfying  $V = V_f + I_c^f V_c$ ) is solved from another Poisson equation  $\nabla^2 V_c = I_f^c R_f$ . The transfer operators  $I_f^c$  and  $I_c^f$  are referred to as *restrictor* and *prolongator*, respectively.

Refs. [50, 51] are classical textbooks on multigrid methods. Introductory material can be found in the recently appeared second edition of the Multigrid tutorial by W. L. Briggs [52].

The full-approximation storage method [40] (FAS) is a standard recipe for nonlinear problems.

Beck *et al.* [30, 53] have applied the FAS eigensolver of Brandt *et al.* [41] for electronic structure calculations of small molecules. Costiner and Ta’asan [54, 55] have made several technical improvements to overcome various obstacles related to the application of the FAS-method in electronic structure calculations. It has also been noted [55, 56] that the FAS-scheme, applicable to nonlinear systems of equations, can be directly applied to the nonlinear Kohn-Sham problem, bypassing the self-consistency iterations. However, according to the authors’ knowledge, none of these methods are yet routinely applied in large-scale electronic structure calculations. When many eigenfunctions are solved simultaneously, the FAS methods may suffer from problems with representing the eigenfunctions accurately on the coarse levels, limiting the number of levels that can be used.

Briggs *et al.* [49, 27] apply a steepest descent method, with a special preconditioner. In the preconditioning step, the Hamiltonian is approximated by the kinetic energy term only – thus they end up solving a Poisson equation in the preconditioning step. The same preconditioner is applied also in the (almost) linear scaling method by Fattebert *et al.* [43]. Mortensen *et al.* [57] apply this preconditioning technique in connection with the DIIS-method (direct inversion in the iterative subspace) in their real-space implementation of the projector augmented wave method.

There are efficient solvers for the matrix eigenproblems arising from the finite-difference or finite-element discretization of the Kohn-Sham equations that do not involve the multigrid concept. Chelikowsky *et al.* [58, 25, 59, 60] have successfully applied iterative diagonalization schemes based on preconditioned Krylov techniques, such as the Lanczos method [61]. Their current implementation uses a preconditioned generalized Davidson algorithm [62]. Some form of a multigrid technique should probably play a role in the optimal preconditioning step of Krylov subspace techniques as well. There exists interesting recent development in the field of preconditioned eigensolvers by A. Knyazev and K. Neymeyr [63, 64].

### 3.1 RQMG method

We have developed a generalization of the so-called Rayleigh quotient multigrid method (RQMG) introduced by Mandel and McCormick [65]. Our generalization is presented in Ref. [5]. In this method the coarse grid relaxation passes are performed so that the Rayleigh quotient calculated on the *fine* grid will be minimized. In this way there is no requirement for the solution to be well represented on a coarse grid and the coarse grid representation problem is avoided. Mandel and McCormick [65] introduced the method for the solution of the eigenpair corresponding to the lowest eigenvalue. We have generalized it to the simultaneous solution of a desired number of lowest eigenenergy states by developing a scheme which keeps the eigenstates separated by the use of a penalty functional, Gram-Schmidt orthogonalization, and subspace rotations.

A basic ingredient of the scheme is a very simple relaxation method called *coordinate relaxation* [66]. Coordinate relaxation is a method of solving the discretized eigenproblem

$$Hu = \lambda Bu \tag{10}$$

by minimizing the Rayleigh quotient

$$\frac{\langle u|H|u\rangle}{\langle u|B|u\rangle}. \tag{11}$$

Above,  $H$  and  $B$  are matrix operators chosen so that the Schrödinger equation discretized on a real-space point grid with spacing  $h$  is satisfied to a chosen order  $O(h^n)$ . In Eq. (11)  $u$  is a vector, containing the values of the Kohn-Sham orbitals at the grid points. In the relaxation method, the current estimate  $u$  is replaced by  $u' = u + \alpha d$ , where the search vector  $d$  is simply chosen to be unity in one grid point and to vanish in all other points, and  $\alpha$  is chosen to minimize the Rayleigh quotient. This leads to a simple quadratic equation for  $\alpha$ . For complex eigenfunctions it is possible to either solve a remarkably complicated coupled pair of quadratic equations for the real and imaginary parts of  $\alpha$ , or to sequentially apply separate coordinate relaxation steps for the real and imaginary parts. A complete coordinate relaxation pass is then obtained by performing the minimization at each point in turn and these passes can be repeated until the lowest state is found with desired accuracy.

Naturally, also the coordinate relaxation suffers from CSD because of the use of local information only in updating  $u$  in a certain point. In order to avoid it one applies the multigrid idea. In the multigrid scheme by Mandel and McCormick [65] the crucial point is that *coarse* grid coordinate relaxation passes are performed so that the Rayleigh quotient calculated on the *fine* grid will be minimized. In this way there is no requirement for the solution to be well represented on a coarse grid. In practice, a coarse grid search substitutes the fine grid solution by

$$u'_f = u_f + \alpha I_c^f e_c, \quad (12)$$

where the subscripts  $f$  and  $c$  stand for the fine and coarse grids, respectively, and  $I_c^f$  a prolongation operator interpolating the coarse grid vector to the fine grid. The Rayleigh quotient to be minimized is then

$$\frac{\langle u_f + \alpha I_c^f d_c | H_f | u_f + \alpha I_c^f d_c \rangle}{\langle u_f + \alpha I_c^f d_c | B_f | u_f + \alpha I_c^f d_c \rangle} = \frac{\langle u_f | H_f u_f \rangle + 2\alpha \langle I_f^c H_f u_f | d_c \rangle + \alpha^2 \langle d_c | H_c d_c \rangle}{\langle u_f | B_f u_f \rangle + 2\alpha \langle I_f^c B_f u_f | d_c \rangle + \alpha^2 \langle d_c | B_c d_c \rangle}. \quad (13)$$

The second form is obtained by relating the coarse grid operators,  $H_c$  and  $B_c$ , with the fine grid ones,  $H_f$  and  $B_f$ , by the Galerkin condition

$$H_c = I_f^c H_f I_c^f; \quad B_c = I_f^c B_f I_c^f; \quad I_f^c = \left( I_c^f \right)^T. \quad (14)$$

Note, however, that the Galerkin condition was not satisfied in our original implementation - instead we discretized the original equation separately on each grid to obtain  $H_c$  and  $B_c$  [discretization coarse grid approximation (DCA)].

The key point to note is that when  $H_f u_f$  and  $B_f u_f$  are provided from the fine grid to the coarse grid, the remaining integrals can be calculated on the coarse grid itself. Thus one really applies coordinate relaxation on the coarse grids to minimize the *fine level* Rayleigh quotient. This is a major departure from the earlier methods, which to some extent rely on the ability to represent the solution of some coarse grid equation on the coarse grid itself. Here, on the other hand, one can calculate the *exact* change in the Rayleigh quotient due to *any* coarse grid change, no matter how coarse the grid itself is. There is no equation whose solution would have to be representable.

Next we consider the generalization of the RQMG method to the simultaneous solution of several ( $N$ ) mutually orthogonal eigenpairs. The separation of the different states is divided into two or

three subtasks. First, in order to make the coarse grid relaxations converge towards the desired state we apply a penalty functional scheme. Given the current approximations for the  $k$  lowest eigenfunctions, the next lowest,  $(k + 1)$ 'th state is updated by minimizing the functional

$$\frac{\langle u_{k+1} | H | u_{k+1} \rangle}{\langle u_{k+1} | B | u_{k+1} \rangle} + \sum_{i=1}^k q_i \frac{|\langle u_i | u_{k+1} \rangle|^2}{\langle u_i | u_i \rangle \cdot \langle u_{k+1} | u_{k+1} \rangle}. \quad (15)$$

The modulus of the overlap integral in the penalty term is squared to make the penalty positive definite. The denominator is required to make the functional independent of the norms of  $u_i$ ,  $i = 1 \dots k + 1$ . The minimization of this functional is equivalent to imposing the orthonormality constraints against the lower  $k$  states, when  $q_i \rightarrow \infty$ . By increasing the shifts  $q_i$  any desired accuracy can be obtained, but in order to obtain a computationally efficient algorithm a reasonable finite value should be used, for example

$$q_i = (\lambda_{k+1} - \lambda_i) + Q, \quad (16)$$

where  $Q$  is a sufficiently large positive constant. In our calculations we have used the value  $Q = 2 \text{ Ha}$ .

The substitution (12) is introduced in the functional (15) and the minimization with respect to  $\alpha$  leads again to a quadratic equation. This time the coefficients contain terms due to the penalty part.

While the penalty functional keeps the states separated on the coarse levels, we apply a simple relaxation method (Gauss-Seidel) on the finest level. The Gauss-Seidel method converges to the nearest eigenvalue, so ideally no additional orthogonalizations would be needed. In practice, however, we use Gram-Schmidt orthogonalizations and subspace rotations. However, the number of fine grid orthogonalizations remains small, for example, in comparison with the conjugate gradient search of eigenpairs employing only the finest grid [26].

## 4 Technical enhancements

### 4.1 Double grid technique

Representing functions with high frequency components on coarse grids has problems, sometimes referred to as *aliasing* (the high frequency components, not representable on the coarse grids, are aliased to lower frequency components), if one simply takes the pointwise values of the continuous functions at each grid point. The most direct way to see this in electronic structure calculations is to monitor the calculated total energy of an atom or a molecule as the system is moved with respect to the grid. Figure 6.16 on page 254 of [8] illustrates this *egg-box effect* in the case of  $\text{CH}_4$  molecule when calculated with the real-space code `octopus`- the total energy varies with an amplitude of 70 meV when the central atom is moved from one grid point to another (the molecule rigidly following the movement). The first cure suggested to this problem was to simply Fourier filter away the high-frequency components of such a function [49, 27]. This, however, may not be the best solution to the problem.

A much more elegant solution was suggested by Ono and Hirose [67]. This scheme applies most directly to the evaluation of the inner products of the wave-function with the non-local

projectors occurring in norm-conserving non-local pseudopotentials or the projector augmented wave (PAW)-method.

A careful and well-documented implementation of the Ono-Hirose scheme was recently made by Mortensen *et al.* in the context of the PAW method [57]. A key factor in this implementation was to use the scheme not only for the projector functions, but as a general recipe to transfer any function defined on a radial atom-centered mesh to the coarse grid where the wave-functions are computed.

In a grid presentation, integrals over space are turned into sums over grid points. In our implementation of the non-local norm-conserving pseudopotentials, we often need to calculate the integral of a localized function, centered on an atom, multiplied by the wavefunction extended over all space. The most obvious example is the projector function  $\xi_{lm}^a(\mathbf{r} - \mathbf{R}^a)$  centered on atom  $a$  at position  $\mathbf{R}^a$  multiplied by an extended wave-function  $\psi_{nc}(\mathbf{r})$  defined by its values at the gridpoints of the computational grid (as indicated by the subscript  $c$ ).

Using  $G$  to index the grid points used for the wave functions and transforming the integral to a sum over grid points with  $V_c$  being the volume per grid point we get

$$P_{lm}^a = V_c \sum_G \xi_{lmG}^a \psi_{nG} = \langle \xi_{lm,c}^a | \psi_{nc} \rangle \quad (17)$$

where  $\psi_{nG} = \psi_n(\mathbf{r}_G)$ , and  $\mathbf{r}_G$  is the position of grid point  $G$  (only grid points in the localized region around atom  $a$  need to be summed over). For  $\xi_{lmG}^a$  we could use  $\xi_{lm}^a(\mathbf{r}_G - \mathbf{R}^a)$ . However, this is not accurate enough, unless we use a very fine grid, which would compromise efficiency. Instead we use the elegant double grid technique of Ono and Hirose [67]. Here we interpolate the wave function to a finer grid  $f$ , and evaluate the inner product there, using pointwise values of the projector function  $\xi_{lm,f}^a$  on the finer grid. It is most convenient in the following discussion to use the prolongator (interpolation) operator  $I_c^f$  and its transpose, the restriction operator  $I_f^c$ .

$$P_{lm}^a = \langle \xi_{lm,f}^a | I_c^f \psi_{nc} \rangle = \langle I_f^c \xi_{lm,f}^a | \psi_{nc} \rangle. \quad (18)$$

Here the relation  $I_c^f = (I_f^c)^T$  (Eq. 14) is used. We see, that the interpolation of the wave function needs not be done in practice. Comparing Eqs. (17) and (18) it is easy to see that

$$\xi_{lm,c}^a = I_f^c \xi_{lm,f}^a, \quad (19)$$

*i.e.* the projector is first evaluated on the auxiliary fine grid (this needs to be done only once in the beginning of the calculation), and then brought to the coarser grid used to represent the wave-functions by the restriction operator. The fine grid can, e.g. be a uniform grid with five times the density of the computation grid, as suggested in Ref. [67]. However, a more economic choice would be to select special integration points corresponding to a Gaussian quadrature for this finer grid, and properly account for the integration weights.

The projector functions are not the only localized atom-centered functions in our implementation of the pseudopotential method. In addition, we have atom centered Gaussian positive charge distributions, used to neutralize the charge density occurring in (Eq. 8), and associated local potential corrections  $\Delta V_{loc} = V_{loc}(r) - Z \text{erf}(r/r_c)/r$ . In practice, we have used the same scheme of evaluating these functions on a fine grid and restricting them to the coarse computational

grid, and found two orders of magnitude reduction in the egg-box effect, as reported also by Mortensen et al. in the case of the PAW scheme [57].

Note, however, that strictly speaking a nonlocal operator on the coarse grid should replace the local potential of the fine grid:

$$\langle I_c^f \psi_{nc} | (\Delta V_f) I_c^f \psi_{nc} \rangle = \langle \psi_{nc} | I_f^c (\Delta V_f) I_c^f \psi_{nc} \rangle. \quad (20)$$

The sparse matrix  $I_f^c (\Delta V_f) I_c^f$  can be constructed in the same way as the Galerkin form  $H_c$  in Section 4.5. A similar accuracy – and similar nonlocal operator replacing the local potential – is obtained if the wave-functions are expanded in the nonorthogonal basis of piecewise polynomial functions associated with the grid points (the finite-element method), and the matrix-elements of the potential in this basis are properly evaluated.

In practice, the simple restriction may be justified, besides by the fact that it seems to work well in practice, also by the fact that we evaluate the density directly from the pointwise values of wave-functions on the coarse grid, and the related correction to the total energy satisfies (note that we use the notation  $\langle f | g \rangle$  as a shorthand for  $\int d\mathbf{r} f^\dagger g$ )

$$\langle I_c^f n_c | \Delta V_f \rangle = \langle n_c | I_f^c (\Delta V_f) \rangle. \quad (21)$$

These relations seem to suggest, that in a numerically correct implementation, a local potential (obtained by simple restriction from the auxiliary fine grid in the double grid scheme) should operate on the density *e.g.* in expressions for the total energy, while the nonlocal form  $I_f^c V I_c^f$  should be used in the eigenvalue problem when operating on the wave-functions. It could be the case that treating the local potential numerically properly, and also computing the density, exchange-correlation potential and electrostatic potential on a grid finer than that used for the wave functions, would allow the use of even coarser grids for the wave-functions, resulting in substantial memory and cpu savings. After all, plane-wave and grid presentations of the wave-functions should in principle be equivalent. Yet the conclusion made in *e.g.* in Ref. [57] is that an order of magnitude more memory is needed to represent the wave-functions on a real-space grid than by storing the plane-wave coefficients.

A possible improvement to the existing methodology would indeed be to evaluate the density on a finer grid (with grid spacing halved):

$$n_f = \sum_i |I_c^f \psi_{i,c}|^2. \quad (22)$$

The Hartree and exchange-correlation potentials would then be evaluated on this finer grid and returned to the coarse, wave-function grid through either the above described method yielding a short-range non-local potential operator, or by the simple restriction which may be accurate enough in practice (or, as suggested above, both of these operators would be needed for different purposes). Note that the use of Eq. (22) requires also a modification for the normalization condition for the wavefunctions,  $(\psi, I_f^c I_c^f \psi) = 1$ . This would be analogous to the plane-wave scheme, where the cutoff wave-vector for the density is twice the cutoff wave-vector for the wave-functions. Such a scheme is not yet implemented in `rspace` (or at least not properly tested), and not in any other real-space method either according to the authors knowledge. Note however that in the PAW-scheme by Mortensen *et al.*, such a finer mesh is used for the solution of the

Poisson equation. However, the relation (22) is not used – instead the density is first evaluated on the coarse grid and then interpolated to the fine grid.

Finally, it would be interesting to see, if the idea can be applied also to the kinetic energy stencil  $T_c$  (or  $A_{\text{meh},c}$  and  $B_{\text{meh},c}$  of section 4.4), by replacing it with  $I_f^c T_f I_c^f$ . Again this could be done using the same algorithm as explained for the  $B$ -stencil in Section 4.5.

We encourage the interested reader to obtain the source code of `rspace` from the web-page [1] (or use his/her own favourite implementation of real-space grid methods) and implement these ideas – there is no guarantee that we will have time to do so in the near future.

## 4.2 Mixing schemes (traditional)

Reaching self-consistency in the solution of the Kohn-Sham equations (1)-(5) can be a tricky task for systems where the Hartree and exchange-correlation potential dominate over the external potential (e.g. quantum dots described in Section 6), and/or when the system size is large (e.g. thousands of electrons as in the axially symmetric jellium model calculations described in Section 7). Defining the output density  $n_{\text{out}}$  as the density obtained from Eq. (2), when the orbitals are solved from Eq. (1) in the potential generated through Eqs. (3)-(5) by the input density  $n_{\text{in}}$ , the simplest stable iteration scheme results by choosing for the input density of the next iteration the linear combination

$$n_{\text{in}}^{\text{next}} = (1 - \kappa)n_{\text{in}} + \kappa n_{\text{out}}. \quad (23)$$

Instead of the density  $n$ , the potential  $V_{\text{eff}}$  can equally well be mixed. In large systems, or quantum dots in low confinement, the mixing parameter  $\kappa$  may have to be chosen smaller than one percent. Clearly more sophisticated mixing schemes should be used.

We have recently implemented the standard Pulay mixing scheme [68, 69] and its several variants. An interesting new variant is the guaranteed reduction Pulay (GRPulay) method [70], where no mixing parameter needs to be given. The key idea of the GRPulay method is, that at the first iteration one computes also the residual of the output density. Then, in the two-dimensional space spanned by the input and output densities, the residual is minimized (assuming a linear dependence between input density and the residual), and the input and output densities for the next iteration are predicted, and the new residual of the output density computed.

A preconditioning to the Pulay scheme that damps the long wavelength changes of the density was proposed by Kerker [71]<sup>2</sup>. Also the use of a special metric that weights long wavelength errors stronger than short wavelength errors was proposed by Kresse and Furthmüller in Refs [10, 11]. In these schemes, a Fourier decomposition of the density to components of different wavelengths is required. We have used the following multigrid-based method to make this decomposition. Here  $N$  denotes the coarsest grid used, so that  $n_N$  is the density component of the longest wavelength.  $I_1^N = I_1^2 \dots I_{N-1}^N$  is the restriction operator from the finest grid 1 to the coarsest grid  $N$ .

$$n_N = I_N^1 I_1^N n \quad (24)$$

---

<sup>2</sup>Note, that the Kerker scheme was originally motivated by a real-space scheme [72, 73, 74], where, instead of the Poisson equation, a modified Helmholtz equation is solved. We have implemented this idea as well, and found it very useful in some calculations.

$$n_{k-1} = I_{k-1}^1 I_1^{k-1} (n - \sum_{i=k}^N n_i). \quad (25)$$

It can be easily seen that this decomposition satisfies  $\sum_{i=1}^N n_i = n$ , and obviously each component  $n_i$  contains features with a wavelength characteristic for level  $i$ . Furthermore, it can be checked that the norm of  $n_N$  is equal to the number of electrons in the charge distribution  $n$ , while the norm of other components is zero.

### 4.3 Response iteration methods

While the mixing schemes referred to above use mainly mathematical tricks in accelerating the convergence towards self-consistency, Auer and Krotscheck [75, 76, 77] have suggested a “physical” method where the static dielectric function of the nonuniform electron gas is utilized to obtain a rapidly converging algorithm. They define the functional  $F[n_{\text{in}}](\mathbf{r}) = n_{\text{out}}[n_{\text{in}}](\mathbf{r}) - n_{\text{in}}$  and obtain the following linear integral equation for the density correction  $\delta n(\mathbf{r})$  to be added to  $n_{\text{in}}$ :

$$F[n](\mathbf{r}) = \int d^3 r' \epsilon(\mathbf{r}, \mathbf{r}'; 0) \delta n(\mathbf{r}'), \quad (26)$$

where

$$\epsilon(\mathbf{r}, \mathbf{r}'; 0) = \delta(\mathbf{r} - \mathbf{r}') - \int d^3 \mathbf{r}'' \chi_0(\mathbf{r}, \mathbf{r}''; 0) V_{\text{p-h}}(\mathbf{r}, \mathbf{r}') \quad (27)$$

is the static dielectric function of non-uniform electron gas,  $\chi_0(\mathbf{r}, \mathbf{r}'; 0)$  is the zero-frequency Lindhard function of the noninteracting system (and can be expressed in terms of the occupied and unoccupied orbitals), and the particle-hole interaction (or hartree-exchange-correlation kernel) is defined as

$$V_{\text{p-h}}(\mathbf{r}, \mathbf{r}') = \frac{e^2}{|\mathbf{r} - \mathbf{r}'|} + \frac{\delta V_{\text{xc}}(\mathbf{r})}{\delta n(\mathbf{r}')} = K_{\text{hxc}}(\mathbf{r}, \mathbf{r}'). \quad (28)$$

In a state-space formulation [76], they obtain the following form for this equation:

$$u(\mathbf{r}) = F[n](\mathbf{r}) - \delta n(\mathbf{r}) = 2 \sum_{p,h} \frac{\phi_p(\mathbf{r}) \phi_h(\mathbf{r})}{\varepsilon_p - \varepsilon_h} \int d^3 \mathbf{r}' d^3 \mathbf{r}'' \phi_p(\mathbf{r}') \phi_h(\mathbf{r}'') V_{\text{p-h}}(\mathbf{r}', \mathbf{r}'') \delta n(\mathbf{r}'') \equiv \sum_{h,p} u_{p,h} \phi_p(\mathbf{r}) \phi_h(\mathbf{r}), \quad (29)$$

where the subscript  $p$  refers to “particle-states” (unoccupied states) and  $h$  refers to “hole-states” (occupied states). In practice, the number of unoccupied states needed for a calculation to converge is often no more than the number of occupied states. Nevertheless, a scheme where only occupied states are required is desirable, and was indeed derived [76] by making the *collective approximation* that the coefficients  $u_{p,h}$  are matrix elements of a *local* function  $\omega(\mathbf{r})$  i.e.

$$u_{p,h} = \int d^3 \mathbf{r} \phi_p(\mathbf{r}) \phi_h(\mathbf{r}) \omega(\mathbf{r}). \quad (30)$$

After some manipulation one arrives at the following equation for  $\tilde{\omega}(\mathbf{r}) = \sqrt{n(\mathbf{r})} \omega(\mathbf{r})$ :

$$[H_0 + 2S_F * \tilde{V}_{\text{p-h}} * S_F] * \tilde{\omega} = 2S_F * \tilde{V}_{\text{p-h}} * \frac{\Delta n}{\sqrt{n}}, \quad (31)$$

where

$$H_0(\mathbf{r}) = \frac{1}{2} \left[ -\nabla^2 + \frac{\nabla^2 \sqrt{n(\mathbf{r})}}{\sqrt{n(\mathbf{r})}} \right], \quad (32)$$

$$\tilde{V}_{p-h} = \sqrt{n(\mathbf{r})}V_{p-h}\sqrt{n(\mathbf{r})} \quad (33)$$

and

$$S_F(\mathbf{r}, \mathbf{r}') = \delta(\mathbf{r} - \mathbf{r}') - \frac{1}{\nu} \frac{1}{\sqrt{n(\mathbf{r})n(\mathbf{r}')}} \sum_{h,h'} \phi_h(\mathbf{r})\phi_h(\mathbf{r}')\phi'_h(\mathbf{r})\phi'_h(\mathbf{r}'), \quad (34)$$

where  $\nu = 2$  for a spin-restricted calculation, and  $\nu = 1$  otherwise. Finally, one obtains the density correction from

$$u(\mathbf{r}) = \sqrt{n(\mathbf{r})}[S_F * \tilde{\omega}](\mathbf{r}). \quad (35)$$

Above  $[A * B](\mathbf{r}, \mathbf{r}')$  denotes the ordinary matrix product defined as  $\int dr'' A(r, r'')B(r'', r')$ , referred to as a *convolution* in Ref. [76]. In collaboration with M. Aichinger, we have implemented the response iteration schemes utilizing both the state-space formulation of the full-response method (Eq. 29) and the collective approximation (Eq. 31) in connection with the `rs2dot` and `cy12` -programs. To solve the integral equations (29) and (31) we have used either the conjugate gradient or the generalized minimum residual (GMRES)-method [78]. In the case of very large systems, a more efficient solver, maybe a multigrid scheme, for Eq. (31) could be useful.

#### 4.4 Higher-order compact discretizations

The Mehrstellen discretized Schrödinger equation

$$H_{\text{Mehr}}\psi_i = A_{\text{Mehr}}\psi_i + B_{\text{Mehr}}(V\psi_i) = \varepsilon_i\psi_i \quad (36)$$

was first introduced to electronic structure calculation by Briggs *et al.* [49, 27]. The matrices of this fourth order discretization only have elements corresponding to the nearest and second nearest neighbor grid points in three-dimensional space. This is in contrast to the traditional central finite difference (CDS) fourth order discretization, which is more nonlocal, and involves thirteen points in a starlike type constellation consisting of three orthogonal line segments of five grid points each. Going to higher order, the CDS stencils become more and more nonlocal [25]. It is argued in [49], that the fourth order Mehrstellen discretization has accuracy comparable to the sixth order CDS-stencil. In addition to the Mehrstellen discretization, we have derived and implemented a set of higher order compact, Mehrstellen type stencils for the Schrödinger and Poisson equations [79].

One immediately notes that although  $B_{\text{Mehr}}^{-1}H_{\text{Mehr}}$  is Hermitian [27],  $H_{\text{Mehr}}$  itself is not. In the original implementation of the RQMG-method [5], Hermiticity of  $H$  and  $B$  is assumed, and this can degrade the performance of the RQMG method when used with Mehrstellen-type stencils. A generalization of the RQMG-method to non-hermitian discretizations is under construction.

#### 4.5 RQMG with Galerkin conditions

As explained in Section 3.1, our original implementation of the RQMG method does not respect the Galerkin conditions of Eq. (14), but replaces the  $H$  and  $B$  matrices on the coarse levels by a rediscrization of the original problem (discretization coarse grid approximation, DCA). This can in some cases result in a limitation of the coarsest level that can be used during the multigrid V-cycle, and hinder the convergence of the higher, unoccupied levels, that are needed in, e.g., the linear-response calculations based on time-dependent DFT (TDDFT) or the full-response

formulation of the response-iteration scheme (See Section 4.3). In practice, convergence for the required number of states can be obtained by selecting a grid dense enough and tuning the coarsest grid size, but in large three-dimensional calculations it is not desirable to have to use dense grids simply because of an improperly implemented numerical scheme.

We have recently implemented also the full Galerkin version of the RQMG method. Note that even for CDS-stencils, for which  $B_f = I$  on the fine level,  $B_c \neq I$  on the coarse level. We note that multiplying a coordinate vector  $e_G$  (which has the value 1 at a single grid point  $G$  and 0 in all other points) by a matrix  $A$  produces the column vector of  $A$  corresponding to the point  $G$ . Then, the column of  $H_c^T$  (the required row of  $H_c$ ) corresponding to  $G$  is given by

$$H_c^T e_G^c = I_f^c H_f^T I_c^f e_G^c. \quad (37)$$

Here,  $e_G$  is first multiplied by  $I_c^f$ , and the (well-known) column vector of the prolongator is obtained. The result is multiplied by the transpose of  $H_f$  (given in stencil representation on the finest level, and compressed row storage (CRS)-format [80] on coarse levels). Finally multiplication with the restriction operator  $I_f^c$  gives the row of the Galerkin  $H_c$ . This vector will be nonzero only in the immediate vicinity of  $G$ , and thus we have obtained a row of the sparse matrix  $H_c$ , to be stored in CRS-format. This scheme is much faster than the more obvious alternative of representing each of the three matrices appearing above in Eq. 37 in CRS format and computing the two matrix products by standard methods. The matrix  $B_c$  is obtained in exactly the same way, but since  $B_f$  is independent of  $\mathbf{r}$ , so will  $B_c$  also be, and this can be stored in the simple stencil format, and is very fast to compute. The current implementation of this scheme is a bit slower than using the stencil representation, but results in guaranteed convergence even on very coarse grids. More speed may be obtained by using the Galerkin matrices only on the very coarse grids, while keeping the CDA on, e.g., the two finest levels. Also, more convenient formats than CRS could result in additional speed - in fact on each row of the matrix the nonzero elements have the same pattern, so that simple array could be a more convenient storage format. Note that the kinetic energy operator still allows a simple stencil representation, as does  $B$  - it is the potential energy which requires the non-local non-stencil form in the Galerkin formulation.

## 4.6 Alternative eigenproblem solvers

It would be desirable to implement a few alternative eigenvalue solvers, in addition to RQMG, in connection with MIKA. For example, the approach chosen by Mortensen *et al.*, to follow as accurately as possible the plane-wave scheme of Kresse *et al.* [10, 11], based on the DIIS-method, only replacing the preconditioning operator by a multigrid V-cycle, seems promising. On the other hand, Krylov subspace methods such as Lanczos or block Davidson are well-known efficient schemes, and careful comparisons between them and the RQMG-method would be interesting. A parallel implementation of the generalized Davidson algorithm is used by Chelikowsky *et al.* [62] to treat three-dimensional systems of up to a thousand electrons. Recently, a new preconditioned, Krylov-space technique has been introduced by A. Knyazev [63, 64] - this method is claimed to be more efficient than its precursors. We have made some comparisons, according to which it seems not to be competitive with RQMG, but more work needs to be done before making

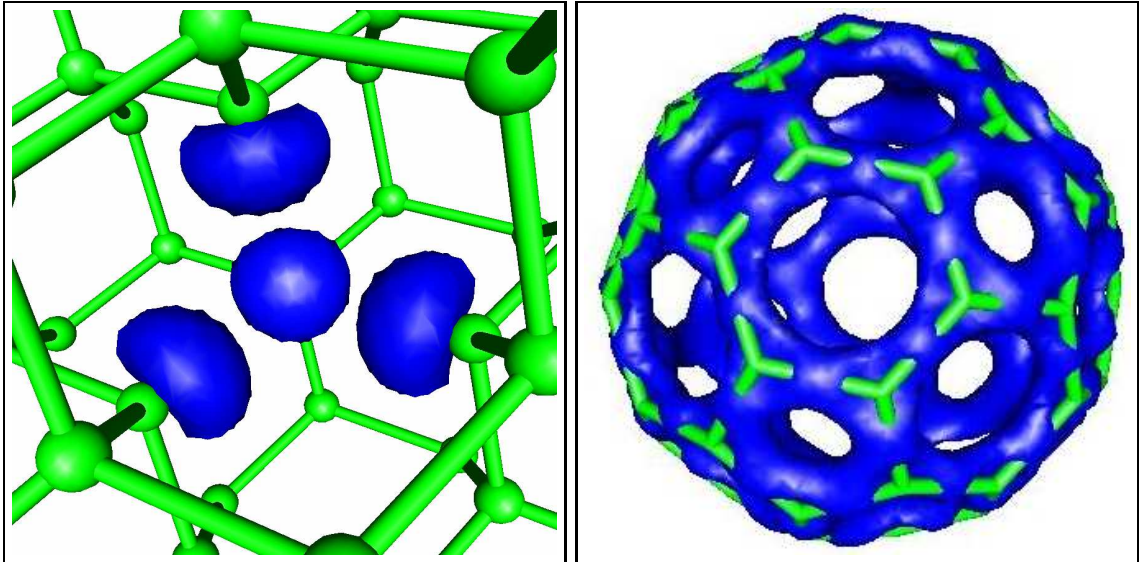


Figure 2: Archtypical applications of electronic structure calculations with periodic and cluster boundary conditions. Left panel: electron density isosurface corresponding to the deep states localized at the neutral, ideal (no ion relaxation) silicon vacancy in Si. Right panel: isosurface of the Kohn-Sham orbital corresponding to the lowest eigenvalue in the  $C_{60}$ -molecule.

a definite conclusion. Auer, Krotcheck and Aichinger [81, 77] have developed a surprisingly efficient scheme based on time evolution in imaginary time with fourth order factorization of the operator  $\exp(-\epsilon H)$ .

## 5 Status of MIKA/rspace

The development of `rspace` has been driven more by individual student projects, Masters projects and technical improvements as described in Section 4 and below than by actual research projects. In principle, nothing prevents the use of the code as it is today in many areas of research. Maybe the most topical field, where real-space grid methods are actively used, is in the applications of the real-time [82] as well as in the linear-response [83] formulations of time-dependent density-functional theory. This field also has a high priority as a future direction in the MIKA-project.

The `rspace` code allows both periodic and cluster boundary conditions. In the cluster case, the boundary values for the Coulomb potential in Eq. (8) are computed by a multipole expansion including terms up to the quadrupole term. In the periodic case, the average potential is set to zero. Boundary conditions for general  $\mathbf{k}$ -points have been implemented. A simple generalization to a combination of cluster boundary conditions in one or two directions and periodic in the other directions would allow computations for surfaces or polymers, respectively, avoiding the periodic images problematic in plane-wave calculations. Even a special boundary condition for long polymers where a unit cell is invariant with respect to a combination of a translation and a rotation about the axis of translation can be implemented in the real-space grid context.

The code has been parallelized through domain decomposition in real-space, and also over the  $\mathbf{k}$ -points. Forces and structural optimization have been implemented - in fact we have two

implementations of structural optimization, one written in `Fortran90` and the other in `Python`. The `Fortran90` implementation has been tested by relaxing the structures of various defects in silicon [84], the results being in agreement with plane-wave calculations.

Recently, the Perdew-Burke-Ernzerhof (PBE) [85] generalized gradient approximation (GGA) has been included in this code - it was taken more or less directly from the other open-source real-space package `octopus` [4]. As a sequel to this small project, we will see if the numerical accuracy of this implementation can be improved by following the advice given by Mortensen *et al.* [57], and computing the potential  $V_{xc}(\mathbf{r}_G)$  exactly as the numerical derivative of the discretized  $E_{xc}$  (where the gradient of the density is evaluated via finite differences) with respect to the density at the grid point at  $\mathbf{r}_G$  - a trick similar to that of White and Bird [86] used in the plane-wave context.

## 6 Quantum dots in 2DEG

### 6.1 Introduction and the model

In the rapidly expanding field of nanotechnology, semiconductor quantum dots (QD) represent basic elements of novel nanoelectronic components. They have dimensions from nanometers to a few microns and contain a controlled number of electrons, typically from one to several thousands. Semiconductor QD's are fabricated with several different methods [87]. The common objective between the techniques is to produce a lateral confinement of the two-dimensional electron gas (2DEG) at the interface of a semiconductor heterostructure, e.g. GaAs/AlGaAs, so that the transverse dimensions are considerably larger than the thickness of the dot. Hence, the corresponding model system is usually two-dimensional, and the shape of the lateral confining potential may be varied at will. The most common approximation is a parabolic confinement which has been shown to model the conventionally fabricated QD's with a reasonable accuracy [88]. In this report, however, we review our results for various geometries that have had manifestation in the experiments.

We define the quantum dot to be located on the  $xy$  plane and use the effective-mass approximation with the material parameters for GaAs, i.e., the effective mass  $m^*=0.067 m_e$  and the dielectric constant  $\epsilon = 12.4 - 13$ . The many-body Hamiltonian for this system in the presence of an external magnetic field can be written in SI units as

$$H = \frac{1}{2m^*} \sum_{i=1}^N [-i\hbar\nabla_i + e\mathbf{A}(\mathbf{r}_i)]^2 + \sum_{i<j}^N \frac{e^2}{4\pi\epsilon_0\epsilon|\mathbf{r}_i - \mathbf{r}_j|} + \sum_{i=1}^N [V_{\text{ext}}(\mathbf{r}_i) + g^* \mu_B B s_{z,i}], \quad (38)$$

where the vector potential is chosen in the symmetric gauge,  $\mathbf{A} = \frac{B}{2}(-y, x, 0)$ . This determines the magnetic field perpendicular to the dot plane, i.e.,  $\mathbf{B} = \nabla \times \mathbf{A} = B\hat{z}$ . The last term is the Zeeman energy, where  $g^*$  is the effective gyromagnetic ratio for GaAs (typically  $-0.44$ ),  $\mu_B$  is the Bohr magneton, and  $s_z = \pm\frac{1}{2}$  for the electron spin  $\sigma = \uparrow, \downarrow$ , respectively. The spin-orbit interaction is excluded in the Hamiltonian, since it is supposed to be relatively small in a wide-gap material like GaAs.

## 6.2 Computational aspects

In the calculations we apply mostly the SDFT in the conventional self-consistent KS formulation. In high magnetic fields we have also employed the computationally more demanding current-spin-density-functional theory (CSDFT), which does not, however, represent a considerable qualitative improvement over the SDFT. A detailed comparison between these two methods for a six-electron quantum dot can be found in Ref. [89].

We have also tested different parametrizations for the exchange-correlation functionals in the LSDA [89]. Quantum Monte Carlo energies for a six-electron QD in zero and finite magnetic fields were taken as benchmark results. According to our calculations, the functional by Ataccalite and co-workers [90] generally gives more accurate results than the form by Tanatar and Ceperley [91]. However, the CSDFT suffers from the lack of accurate interpolation forms between the zero and high-field limits for a given spin polarization.

In our QD program `rs2dot`, the RQMG-method is used for solving the effective single-electron Schrödinger equation on a two-dimensional point grid. In practical calculations, the number of grid points is set between 80 and 128 in one direction. This gives  $\sim 1$  nm for a typical grid spacing, which is sufficient for describing electrons in GaAs, and the discretizations are of the 4th order. The accuracy of the calculations has been checked with the Richardson extrapolation, leading to a typical error of less than  $\sim 1\%$  in the total energy ( $\lesssim 3\%$  in the low-density limit). A converged solution typically takes 100...500 self-consistency iterations, but that number could be remarkably reduced by using the density-response functions [75, 76, 77] which are currently implemented into the present method.

## 6.3 Zero-field results

As a symmetry-unrestricted method the real-space approach is suitable for treating QD's defined by a non-circular confining potential. In zero magnetic fields we have studied Wigner crystallization in polygonal systems [92], namely, how the electrons localize into a regular lattice at sufficiently low densities as the dot size is increased. The phenomenon is due to the different scalings of the potential and kinetic parts of the total energy. The former part becomes gradually dominant over the latter as the density decreases, and finally the kinetic energy remains in the zero-point motion of the vibrational modes.

For two-electron polygonal QD's, we find the Wigner-molecule formation as the density parameter  $r_s = \sqrt{A/(N\pi)} \approx 3$ , where  $A$  is the area of the polygonal potential well. This agrees well with the exact diagonalization (ED) results by Creffield *et al.* [93]. The qualitative behavior in the electron density is similar in both DFT and ED, leading to the localization to the corners of the QD as  $A$  increases (see Fig. 3). For  $N > 2$ , we find the formation of extra density peaks along the sides of the QD. In the case of a double number of electrons with respect to the number of corners in the dot, the enlargement of the dot area leads to  $N$  density peaks at  $r_s \simeq 4.0$  in all polygonal QD's studied. This value is defined as the critical density parameter for the Wigner crystallization in those systems.

In Ref. [94] we have presented a detailed study on the electronic structure of rectangular QD's

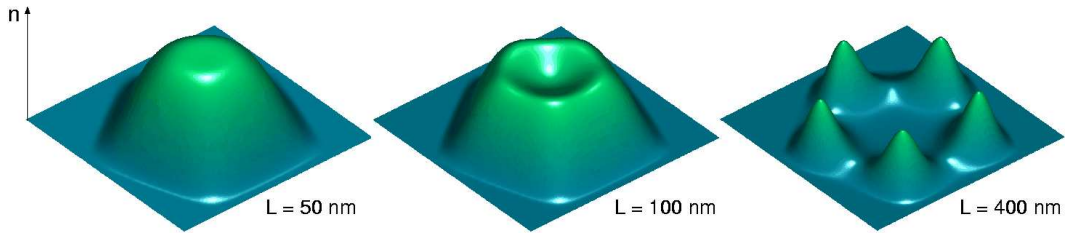


Figure 3: Electron densities for three different sizes of a pentagonal two-electron quantum dot. As the size of the dot increases, the electrons localize in the corners and form a Wigner molecule.

with a hard-wall confinement potential similar to the above presented polygonal system, i.e.,

$$V_{\text{ext}}(x, y) = \begin{cases} 0, & 0 \leq x \leq \beta L, 0 \leq y \leq L \\ \infty, & \text{elsewhere.} \end{cases} \quad (39)$$

The deformation parameter  $\beta$  thus determines the ratio between the side lengths of the rectangle, and the area of the rectangle is set to  $\beta L^2 = \pi^2 a_B^{*2} \approx 1000 \text{ nm}^2$ .

The chemical potentials and the addition energies are calculated as a function of  $\beta$  with both the SDFT and variational quantum Monte Carlo method. The agreement between the two methods is very precise. In addition, the comparison of our results with the experiments and previous simulations [95] shows that the hard-wall approximation is slightly more realistic than the elliptic one. However, more experimental data over a wider range of  $\beta$  would be needed.

As a result of Hund's rule, we find several partially spin-polarized states with  $S = 1$  as  $\beta$  and  $N$  are varied. In the SDFT those states are bracketed by spin-density waves where the spin-up and spin-down densities are symmetrically coupled with each other. In Ref. [96], we have proven explicitly, that those states represent a wrong mixing of different spin states. The underlying problem is the fact that the SDFT can not properly describe ensemble- $v$ -representable densities, i.e., systems with more than one major configuration in the ground-state wave function.

#### 6.4 Magnetic fields and the vortex clusters

The solutions in high magnetic fields predict the existence of a completely spin-polarized finite structure called the maximum-density droplet (MDD). The MDD is related to the quantum Hall effect with one completely filled Landau level, i.e., the filling factor  $\nu = 1$ , and its existence has also been verified experimentally [97]. The MDD state can be found in various QD geometries. In the MDD state of a circular QD, electrons occupy successive angular momentum levels from  $l = 0$  to  $l = -N + 1$ , where  $N$  is the number of electrons in the dot. The MDD state is stable for a rather wide range of the magnetic field, but at a certain field strength it reconstructs into a lower-density droplet (see below).

In Ref. [98] we study the MDD formation in non-circular hard-wall QD's defined as above. We identify the MDD window in the calculated chemical potentials  $\mu(N)$ . In addition, we predict the onset of the MDD from the number of flux quanta  $N_\Phi$  penetrating through the QD and find a good agreement with the kinks in the chemical potentials (see Fig. 4). Due to the Coulomb interactions, the MDD electron density in a hard-wall dot is pronouncedly localized in

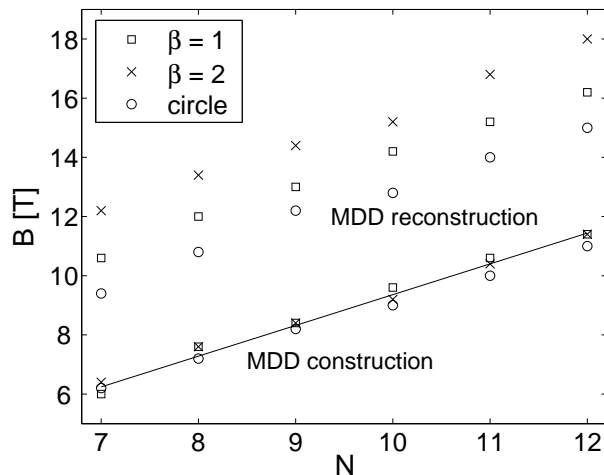


Figure 4: MDD-window limits obtained from the kinks in  $\mu(N)$  as a function of  $N$  in different QD geometries. The line shows the prediction for the MDD formation, based on the number of flux quanta penetrating the dot.

the corners and on the edges, in contrast with the parabolic case that exhibits a smooth density distribution [99].

When the magnetic field is further increased the MDD-state breaks down to a lower density droplet. The mechanism of this breakdown has been a focus of much theoretical and experimental work. Recently, we have calculated beyond-MDD states of different QD's. SDFT predicts formation of vortex structures, i.e. holes in the charge density associated with rotating currents around them [100]. They can be seen directly in the total electron density obtained by our symmetry-unrestricted approach. However, these symmetry breaking solutions do not give the physical particle density in the laboratory frame of reference (since it must remain rotationally symmetric) but it may reveal electron-electron correlations in the true many-body wave function which is inaccessible in the density-functional approach. Detailed calculations using exact many-body methods lead to similar vortex structures, giving credence to the interpretation of the SDFT results [100].

Using different symmetry-breaking QD geometries it was found that the vortices are stable in high magnetic fields and they correspond to density minima also in the ED results [101]. The vortex formation is a considerable energetic effect and it could be observed in transport experiments similar to those of Oosterkamp *et al.* [97].

Vortex solutions were analyzed further using conditional wave functions in both the ED and the SDFT [102]. The results show that there are two types of vortices: vortices which are on top of an electron and additional vortices which are not bound to a particular electron (see Fig. 5). For the correct particle statistics (Fermion antisymmetry) the number of vortices on top of each electron must be odd. The off-electron vortices were found to give rise to charge minima associated with rotating currents around them. The vortex formation reduce the interaction energy and cause strong correlations between the electrons. Some of the solutions have much in common with the fractional quantum Hall states. For instance, the solution with three vortices near each electron was identified as a finite size precursor of the  $\nu = 1/3$  fractional quantum Hall

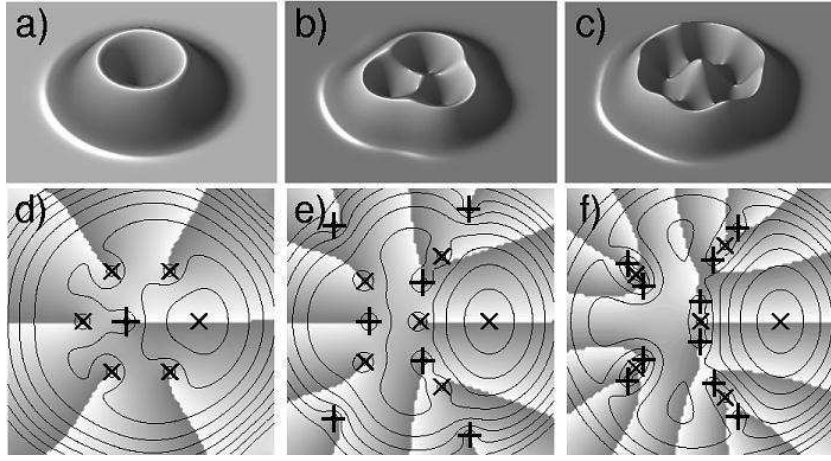


Figure 5: (a-c) Vortex holes in the density-functional electron density of six-electron quantum dots and (d-f) the corresponding conditional wave functions in the exact diagonalization. The fixed electrons are marked with crosses. The shading shows the wave-function phase which changes by  $2\pi$  in a path around a vortex. There are vortices on top of each electron and additional vortices moving between the electrons (+ signs). The rightmost solution is related to the the  $\nu = 1/3$  quantum Hall state with three vortices near each electron.

state [see Fig. 5(c) and (f)]. Moreover, there appear many similarities between vortex formation in bosonic and fermionic case, suggesting that the vortex formation is a universal phenomenon in 2D quantum systems [103].

## 6.5 Impurities in quantum dots

Theoretical modeling of quantum dots is usually based on the approximation of clean samples, although in real semiconductor devices the effects due to impurities or donor scattering centers may be remarkable. In Ref. [104], a measured transport spectrum of a vertical QD is shown to have clear deviations from the FD energies. We model the system with an external potential consisting of a parabolic confinement and a negatively charged Coulombic impurity placed in the vicinity of the QD. As demonstrated in Fig. 6, the model leads to a good agreement between the calculated single-electron eigenenergies and the experimental spectrum. We also show with the SDFT that in the high magnetic field regime the increasing electron number reduces the distortion induced by the impurity.

## 7 Nanophysics in axial symmetry

In Refs.[105, 106, 107], we have applied the RQMG-method in various nanostructure studies. We found it convenient in all these projects to use axially symmetric model systems instead of atomistic models. This approximation reduces the computational demands and allows us to study rather large systems encompassing hundreds (Refs. [105, 107]) and even thousands (Ref. [106]) of electrons. In addition, by restricting the geometry to the axial symmetry and resorting to jellium models, many random effects related to the detailed and sometimes unimportant

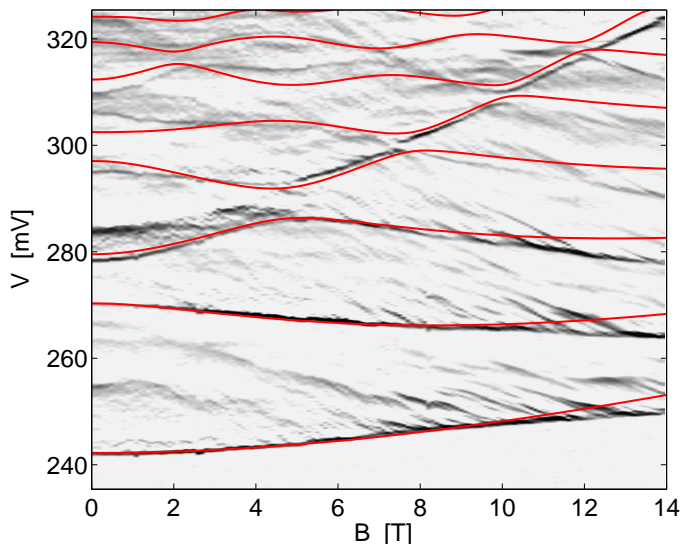


Figure 6: Measured transport spectrum (gray scale) of a GaAs/AlGaAs QD and the calculated single-electron energies (red lines) corresponding to the model potential given in Ref. [98].

atomic structure disappear, and the relevant physics is easier to extract from the simulations.

In the axial symmetry, Eq. (1) for the Kohn-Sham orbital

$$\psi_{m\mathbf{k}n}(\mathbf{r}) = e^{im\phi}U_{m\mathbf{k}n}(r, z) \quad (40)$$

can be replaced by the following equation

$$-\frac{1}{2} \left( \frac{1}{r} \frac{\partial}{\partial r} + \frac{\partial^2}{\partial r^2} - \frac{m^2}{r^2} + \frac{\partial^2}{\partial z^2} + 2V_{\text{eff}} \right) U_{m\mathbf{k}n}(r, z) = \varepsilon_{m\mathbf{k}n} U_{m\mathbf{k}n}(r, z). \quad (41)$$

We denote the components of the  $\mathbf{k}$ -vector by  $k_z$  and  $k_{\parallel}$ . The  $z$ -component  $k_z$  of the  $\mathbf{k}$ -vector only has relevance in periodic systems, such as the nanowires studied in Ref. [107]. In the periodic case, the following Bloch boundary condition

$$U_{m\mathbf{k}n}(r, z + L_{\text{cell}}) = e^{ik_z L_{\text{cell}}} U_{m\mathbf{k}n}(r, z) \quad (42)$$

is satisfied. The radial component  $k_{\parallel}$  enters in Ref. [106], where we approximate a planar system by a hexagonal lattice of circles. We see that the numerical problem is reduced to a two-dimensional one. Furthermore, the problem is conveniently split into a number of independent subproblems - a property which can be exploited in a massively parallel computer environment. The Kohn-Sham orbitals with different  $(m, \mathbf{k})$  (or  $(m, \mathbf{k}, s)$ , should we treat spin-polarized systems) are automatically orthogonal, and can be solved simultaneously.

## 7.1 Ultimate jellium model for a breaking nanowire

In Ref. [107], we have studied the stability of nanowires and the nanowire breaking process performing self-consistent calculations within the ultimate jellium model. In this model, electrons and positive background charge acquire the optimal density minimizing the total energy. The model enables thus studies of shape-dependent properties of nanoscopic systems such as

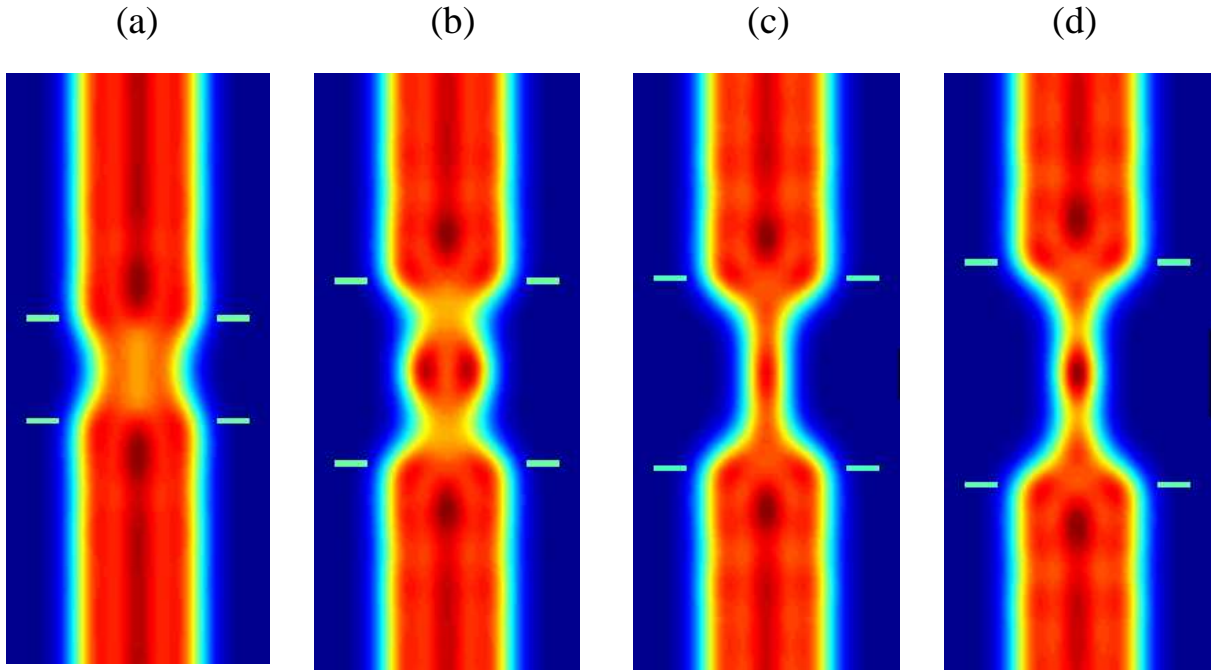


Figure 7: Snapshots from a simulation of nanowire breaking by the ultimate jellium model. A catenoid surface (a), cluster-derived structures (b) and (d), and uniform cylindrical shape (c) can be seen. Green rectangles mark the lead-constriction boundary.

quantum dots or, as in the present work, quantum wires. The model advocates the idea that the electronic structure determines via the shell structure, the geometry and ionic structure also in a partially confined system.

First, we have analyzed the stability of infinite periodic quantum wires pointing out the ability of the electronic band structure to stabilize the nanowires at magic radii, *i.e.* any small deformation of the nanowire along the  $z$  axis always increases the energy. At the unstable radii corresponding to maximum values in the energy oscillations, the wire is uniform up to a critical value of the unit cell length. The critical values found are close to  $L_{\text{cell}}/R = 4.5$ . Above this limit the local energy minimum disappears and a deformation of the wire lowers the total energy. This length is shorter than the classically expected  $2\pi$  value, thus the wire electronic structure also has a destabilizing effect.

Then we have investigated the elongation process of finite nanowires between two leads. The elongation force, conductance and effective radius of the constriction have been calculated simultaneously. The importance of the charge relaxation in order to obtain results in agreement with experiments has been shown, *e.g.*, in the case of the elongation force. The ability of the ultimate jellium (electron density) to acquire the optimal shape allows the selection of magic radii wires that stabilize the nanocontact, as well as the formation of cluster derived structures (CDS) showing the importance of electron states in the formation of these structures. The related resonance states and their origin was also shown. We have found CDS's that can be linked with the eight- and two-electron free-standing clusters.

In summary, three different types of nanocontact stabilization mechanisms have been found

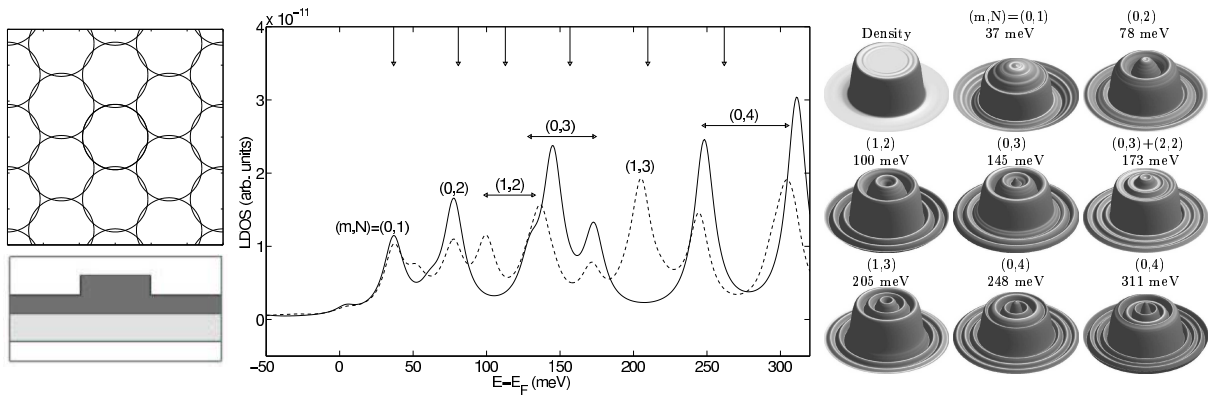


Figure 8: Top left: Hexagonal lattice of area-covering circles. Bottom left: Schematic view of the background charge density in a plane containing the  $z$ -axis in our two-density model for a quantum-dot on top of a full monolayer of Na on Cu(111). Middle: Local density of states on top of a cylindrical QD of 550 electrons on two-jellium substrate calculated at a height of  $18 a_0$  above the jellium edge at the axis (solid line) and at  $r = 20a_0$  (dashed line). The (shifted) experimental peak positions are given by vertical arrows pointing downwards. The peaks are identified with  $(m, N)$  resonance states having two horizontal node planes in the QD. Right: Calculated isosurfaces of the electron density (upper left corner) and LDOS at the energies corresponding to the dominant peaks of the middle panel.

during the breaking process: catenoid-like shape stabilized by classical *surface tension*, straight magic wires stabilized by the *wire electronic shell structure* and CDS's stabilized by *cluster electronic shell structure*.

## 7.2 Adsorbed Na quantum dots on Cu(111)

In Ref. [106], we model electronic properties of the second monolayer Na adatom islands (quantum dots) on the Cu(111) surface covered homogeneously by the wetting layer of one monolayer of Na. An axially-symmetric three-dimensional jellium model, taking into account the effects due to the first Na monolayer and the Cu substrate, has been developed. The model enables the study of systems consisting of thousands of Na-atoms.

We have modeled quantum dots as small cylindrical jellium islands, and the underlying Na monolayer and Cu substrate as a two-density jellium slab. The two parameters of the model have been chosen to fit experimental spectroscopic data and calculated first-principles band structures for one and two completed monolayers of Na on the Cu(111) surface.

The calculated results are compared with experimental findings in scanning tunneling microscopy and photoemission experiments. The model gives local densities of states which are in a quantitative agreement with constant current topographs and  $dI/dV$  spectra and maps. Thereby the idea of surface states which are localized as resonances at the quantum dots is supported. The future applications of the model will include studies of the adsorption and dissociation of molecules in the vicinity of alkali metal quantum dots.

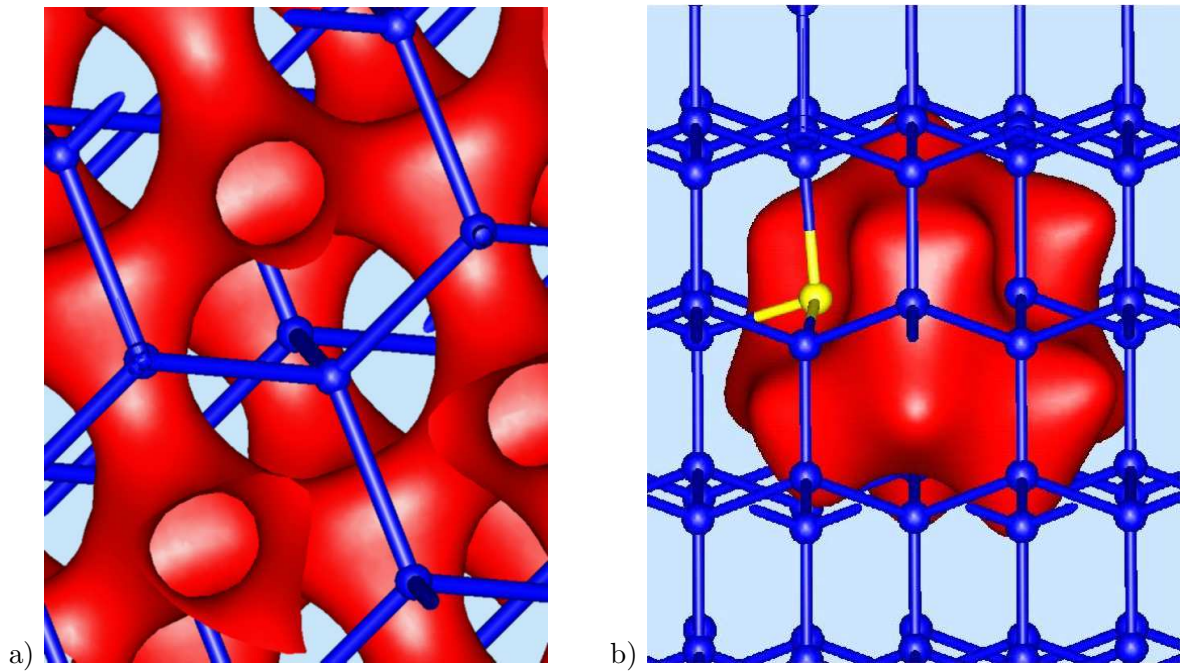


Figure 9: a) An isosurface of the positron wave function in a perfect Si lattice. The positions of the Si atoms are denoted by blue spheres, and the electronic interatomic bonds as blue sticks. The positron lifetime in this state is according to experiments and theory about 220 ps. b) An isosurface of the positron wave function at a vacancy surrounded by one Sb impurity. The Sb atom is denoted by a yellow sphere. The positron lifetime in this state is according to theory about 230 ps.

## 8 Positron calculations

The use of positron annihilation in defect studies is based on the trapping of positrons from a delocalized bulk state to a localized state at the defect (see Fig. 9). The trapping is due to the reduced nuclear repulsion at the open-volume defects. Because the electronic structure seen by the positron at the defect differs from that in the perfect bulk crystal the annihilation characteristics change. The positron lifetime increases because the average electron density decreases. For the same reason the momentum distribution of annihilating electron-positron pairs becomes more peaked at low momenta (see Fig. 10a). However, the positron density may sample the different atomic species of a compound material with different relative probabilities in the bulk and at a defect. The defect may be surrounded by impurity atoms. In these cases the high-momentum region of the distribution, which is mainly due to annihilations with core electrons, reflects the chemical structure of the defect (see Fig. 10b). The changes in the bond structure between the atoms neighboring the defect may also affect the low-momentum part of the distribution. In order to understand these changes and fully benefit from them in defect identification, theoretical calculations with high predictive power are indispensable.

The description of the electron-positron system can be formulated as a two-component density-functional theory [111]. In the measurements there is only one positron in the solid sample at the time. Therefore the density-functional scheme has to be properly purified from positron self-interaction effects. Comparisons with the two-component and experimental results have shown

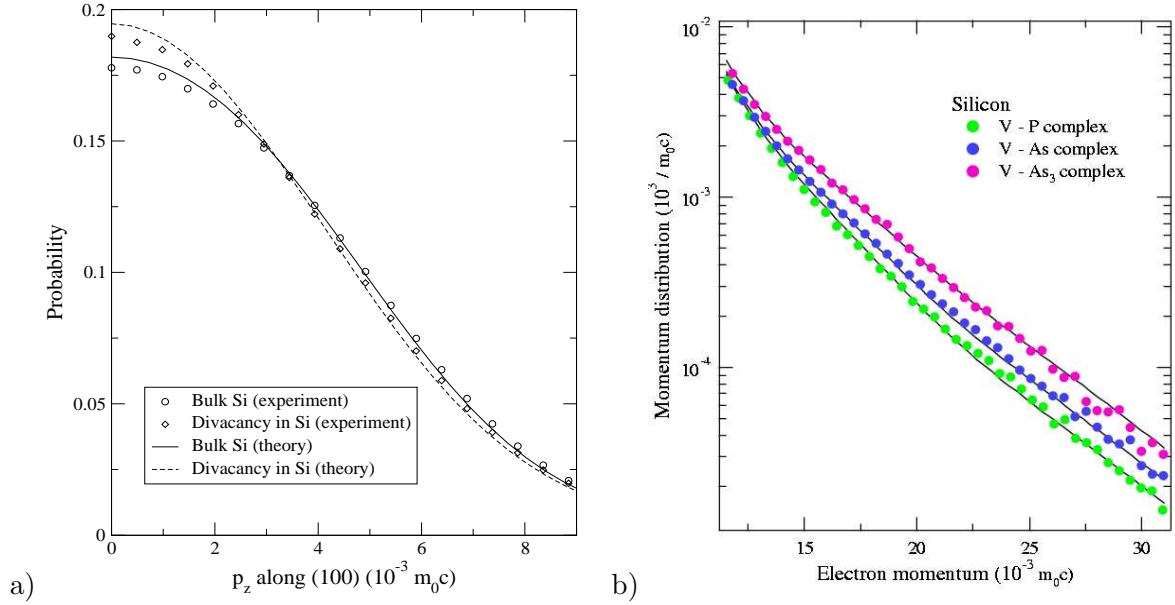


Figure 10: Momentum distributions of annihilating electron-positron pairs in Si. a) Low momentum parts. The theoretical predictions [108] (lines) are compared with the spectra measured by the Doppler broadening technique (markers) [109]. b) High-momentum parts (K. Saarinen *et al.* [110]). The theoretical predictions (solid lines) are compared with the spectra measured by the Doppler broadening techniques (markers). The comparison identifies vacancy-P complexes in electron-irradiated P-doped Si (green circles), vacancy-As complexes in electron-irradiated As-doped Si (blue circles), and vacancy-As<sub>3</sub> complexes in as-grown highly As-doped Si (red circles). The annihilation with As 3d electrons raises the intensity. The study concludes that the saturation of the free electron density in highly As-doped Si is mainly caused by the formation of vacancy-As<sub>3</sub> complexes.

that the following scheme is adequate. First the electron density  $n(\mathbf{r})$  of the system is solved without the effect of the positron. This can be done using different (all-electron) electronic structure calculation methods. A surprisingly good approximation for the positron lifetime and core-electron momentum calculations is to simply superimpose free atom charges. Then the potential  $V_+(\mathbf{r})$  felt by positron is constructed as a sum of the Coulomb potential  $\phi(\mathbf{r})$  and the so-called correlation potential  $V_{corr}(\mathbf{r})$  which is treated in a local density approximation, i.e.

$$V_+(\mathbf{r}) = \phi(\mathbf{r}) + V_{corr}(n_-(\mathbf{r})), \quad (43)$$

The ensuing single-particle Schrödinger equation can be solved using similar techniques as the electron states. For example, we use the three-dimensional real-space Schrödinger equation solver of the MIKA package.

When the electron density  $n(\mathbf{r})$  and the positron density  $n_+(\mathbf{r}) = |\psi^+(\mathbf{r})|^2$  are known the positron annihilation rate is calculated within the LDA as an overlap integral

$$\lambda = \pi r_0^2 c \int d\mathbf{r} n_+(\mathbf{r}) n_-(\mathbf{r}) \gamma(n_-(\mathbf{r})), \quad (44)$$

where  $r_0$  is the classical electron radius,  $c$  the speed of light, and  $\gamma$  the enhancement factor taking into account the pile-up of electron density at the positron (a correlation effect). The inverse of the annihilation rate is the positron lifetime.

The momentum distribution of the annihilating electron-positron pairs is calculated as

$$\rho(\mathbf{p}) = \pi r_0^2 c \sum_j \left| \int d\mathbf{r} e^{-i\mathbf{p}\cdot\mathbf{r}} \psi^+(\mathbf{r}) \psi_j(\mathbf{r}) \sqrt{\gamma(n_-(\mathbf{r}))} \right|^2. \quad (45)$$

Good results, especially for high-momentum part due to the core electrons, are obtained using a state-dependent constant enhancement factor by replacing  $\gamma(n_-(\mathbf{r}))$  above with a constant  $\gamma_j$ , which is determined from the annihilation rate of the state  $j$  [112]. It is this state-dependent form, which we use in practice.

The `doppler`-program delivered within the MIKA package uses the atomic superposition method. The scheme cannot be used for the low-momentum part due to valence electrons. For that purpose self-consistent all-electron wavefunctions have to be constructed. For example, we have used the projector augmented-wave (PAW) method implemented in the plane-wave code VASP [10, 11, 113, 114].

## 9 Summary and outlook

We have given an overview of the real-space, multigrid-based program package called MIKA, and several examples of its applications in research of quantum dots, nanostructures and positron physics. We hope that the work invested in developing these codes could be useful to a wider group of researchers than our own. Therefore, following the model given e.g. by the `octopus`-project [4], and advocated by the `fsatom`-project [2], we have decided to license the code with the GNU general public license (GPL), and distribute the software on a web-page [1]. This does not mean, that we claim our codes to be easy to use or of commercial quality, neither does

it include any promise of user support. On the contrary, we hope that other researchers will take parts of the code, inspect them critically, modify them for their purposes, and distribute the derived product further. Such a distributed mode of development should accelerate the development and adoption of real-space methods in our community.

## 10 Acknowledgements

We are grateful to J. J. Mortensen, M. Marques, A. Castro and J. Wang for useful discussions on real-space methods, to M. Aichinger and E. Krotscheck for collaboration in the implementation of the response iteration technique to the MIKA-package, and to J. J. Mortensen and M. Aichinger for sharing their manuscripts [57, 77] prior to publication. B. Hellsing and N. Zabala are acknowledged for collaboration in the research reported in Section 7. M. Hakala, A. Harju, V. Lehtola, V. Ranki, S. Riikonen, K. Ritvanen, P. Valminen and T. Hakala are acknowledged for their contributions to the MIKA-package through individual student projects, Masters projects or other activity. S. F. McCormick, M. Lyly, J. Ruokolainen, T. Eirola, M. Huhtanen and A. Knyazev are acknowledged for discussions on numerical methods. There should be more such discussions between researchers in the (emerging) real-space electronic structure community and specialists in numerical methods. A. Harju deserves a special acknowledgement for providing us results from accurate many-particle methods and also for constructive criticism on density-functional theory in general and the MIKA-package in particular. Special thanks are due to M. Heiskanen for his original development of the multigrid subroutines. Apologies to those people, whose names should have appeared above, but have been accidentally left out.

## References

- [1] <http://www.csc.fi/physics/mika>.
- [2] <http://fsatom.org>; <http://www.tddft.org/fsatom>.
- [3] <http://www.abinit.org>.
- [4] <http://www.tddft.org/programs/octopus>.
- [5] M. Heiskanen, T. Torsti, M. Puska, and R. Nieminen, Phys. Rev. B **63**, 245106 (2001).
- [6] E. Ogando, N. Zabala, E. V. Chulkov, and M. J. Puska, Phys. Rev. B **69**, 153410 (2004).
- [7] E. Ogando, N. Zabala, E. V. Chulkov, and M. J. Puska, submitted to Phys. Rev. B (2004).
- [8] F. Nogueira, A. Castro, and M. Marques, in *A Primer in Density Functional Theory*, edited by C. Fiolhais, F. Nogueira, and M. Marques (Heidelberg, 2003), 218–256.
- [9] M. C. Payne, M. P. Teter, D. C. Allan, T. A. Arias, and J. D. Joannopoulos, Rev. Mod. Phys. **64**, 1045 (1992).
- [10] G. Kresse and J. Furthmüller, Phys. Rev. B **54**, 11169 (1996).

- [11] G. Kresse and J. Furthmüller, *Comp. Mat. Sci.* **6**, 15 (1996).
- [12] R. Car and M. Parrinello, *Phys. Rev. Lett.* **55**, 2471 (1985).
- [13] R. N. Barnett and U. Landman, *Phys. Rev. B* **48**, 2081 (1993).
- [14] B. Delley, *J. Chem. Phys.* **113**, 7756 (2000).
- [15] G. te Velde, F. Bickelhaupt, E. Baerends, C. F. Guerra, S. van Gisbergen, J. Snijders, and T. Ziegler, *J. Comput. Chem.* **22**, 931 (2001).
- [16] R. Ahlrichs and M. V. Arnim, in *Methods and Techniques in Computational Chemistry: METECC-95*, edited by E. Clementi and G. Corongiu (1995).
- [17] High Performance Computational Chemistry Group, NWChem, A Computational Chemistry Package for Parallel Computers, Version 4.1 (2002), Pacific Northwest National Laboratory, Richland, Washington 99352, USA.
- [18] J. M. Soler, E. Artacho, J. D. Gale, A. García, J. Junquera, P. Ordejón, and D. Sánchez-Portal, *J. Phys. : Condens. Matter* **14**, 2745 (2002).
- [19] T. L. Beck, *Rev. Mod. Phys.* **72**, 1041 (2000).
- [20] S. R. White, J. W. Wilkins, and M. P. Teter, *Phys. Rev. B* **39**, 5819 (1989).
- [21] J. Pask, B. Klein, C. Fong, and P. Sterne, *Phys. Rev. B* **135**, 1 (1999).
- [22] E. Tsuchida and M. Tsukada, *Phys. Rev. B* **52**, 5573 (1995).
- [23] E. Tsuchida and M. Tsukada, *J. Phys. Soc. Jap.* **67**, 3844 (1998).
- [24] K. Tagami, E. Tsuchida, and M. Tsukada, *Surf. Sci.* **446**, L108 (2000).
- [25] J. R. Chelikowsky, N. Troullier, K. Wu, and Y. Saad, *Phys. Rev. B* **50**, 11355 (1994).
- [26] A. P. Seitsonen, M. J. Puska, and R. M. Nieminen, *Phys. Rev. B* **51**, 14057 (1995).
- [27] E. L. Briggs, D. J. Sullivan, and J. Bernholc, *Phys. Rev. B* **54**, 14362 (1996).
- [28] F. Ancilotto, P. Blandin, and F. Toigo, *Phys. Rev. B* **59**, 7868 (1999).
- [29] Y.-G. Jin, J.-W. Jeong, and K. Chang, *Physica B* **274**, 1003 (1999).
- [30] J. Wang and T. L. Beck, *J. Chem. Phys.* **112**, 9223 (2000).
- [31] U. V. Waghmare, H. Kim, I. J. Park, N. Modine, P. Maragakis, and E. Kaxiras, *Comp. Phys. Comm.* **137**, 341 (2001).
- [32] T. A. Arias, *Rev. Mod. Phys.* **71**, 267 (1999).
- [33] D. Bai and A. Brandt, *SIAM J. Sci. Stat. Comput.* **8**, 109 (1987).
- [34] E. J. Bylaska, S. R. Kohn, S. B. Baden, A. Edelman, R. Kawai, M. E. G. Ong, and J. H. Weare, in *Proceedings of the 7th SIAM Conference on Parallel Processing for Scientific Computing*, edited by D. H. Bailey *et al.* (1995), 219.

- [35] J.-L. Fattebert, *J. Comput. Phys.* **149**, 75 (1999).
- [36] F. Gygi and G. Galli, *Phys. Rev. B* **52**, R2229 (1995).
- [37] I. Babuska and Rheinboldt, *Int. J. Num. Meth. Engng.* **12**, 1579 (1978).
- [38] I. Babuska and B. Szabo, *Int. J. Num. Meth. Engng.* **18**, 323 (1982).
- [39] I. Babuska and M. Suri, *Comp. Meth. Appl. Mech. Engng.* **80**, 5 (1990).
- [40] A. Brandt, *Math. Comput.* **31**, 333 (1977).
- [41] A. Brandt, S. F. McCormick, and J. W. Ruge, *SIAM J. Sci. Comput. (USA)* **4**, 244 (1983).
- [42] S. Goedecker, *Rev. Mod. Phys.* **71**, 1085 (1999).
- [43] J.-L. Fattebert and J. Bernholc, *Phys. Rev. B* **62**, 1713 (2000).
- [44] A. D. Becke, *J. Chem. Phys* **76**, 6037 (1982).
- [45] A. D. Becke, *Phys. Rev. A* **33**, 2786 (1986).
- [46] L. Laaksonen, P. Pyykkö, and D. Sundholm, *Comp. Phys. Rep.* **4**, 313 (1986).
- [47] D. Sundholm, *Comp. Phys. Comm.* **49**, 409 (1988).
- [48] J. Kobus, L. Laaksonen, and D. Sundholm, *Comp. Phys. Comm.* **98**, 346 (1996).
- [49] E. L. Briggs, D. J. Sullivan, and J. Bernholc, *Phys. Rev. B* **52**, R5471 (1995).
- [50] W. Hackbush, *Multi-Grid Methods and Applications* (Springer-Verlag, Berlin, 1985).
- [51] P. Wesseling, *An Introduction to Multigrid Methods* (John Wiley & Sons, Inc., New York, 1992).
- [52] W. L. Briggs, V. E. Henson, and S. F. McCormick, *A Multigrid Tutorial, Second Edition* (SIAM, 2000).
- [53] T. L. Beck, K. A. Iyer, and M. P. Merrick, *Int. J. Quantum Chem.* **61**, 341 (1997).
- [54] S. Costiner and S. Ta'asan, *Phys. Rev. E* **51**, 3704 (1995).
- [55] S. Costiner and S. Ta'asan, *Phys. Rev. E* **52**, 1181 (1995).
- [56] J. Wang and K. Marthinsen, Unpublished (2003).
- [57] J. J. Mortensen, L. B. Hansen, and K. W. Jacobsen, submitted to *Phys. Rev. B* (2004).
- [58] J. R. Chelikowsky, N. Troullier, and Y. Saad, *Phys. Rev. Lett.* **72**, 1240 (1994).
- [59] X. Jing, N. Troullier, D. Dean, J. R. Chelikowsky, K. Wu, and Y. Saad, *Phys. Rev. B* **50**, 12234 (1994).
- [60] J. R. Chelikowsky, X. Jing, K. Wu, and Y. Saad, *Phys. Rev. B* **53**, 12071 (1996).

- [61] G. H. Golub and C. F. V. Loan, *Matrix Computations* (The Johns Hopkins University Press, London, 1989), second edition.
- [62] A. Stathopoulos and S. Ögüt and Y. Saad and J. Chelikowsky and H. Kim, *Comput. Sci. Eng.* (2000).
- [63] A. Knyazev, *Siam. J. Sci. Comput.* **23**, 517 (2001).
- [64] A. Knyazev and K. Neymeyr (2003).
- [65] J. Mandel and S. McCormick, *J. Comput. Phys.* **80**, 442 (1989).
- [66] J. L. B. Cooper, *Q. Appl. Math.* **6**, 179 (1948).
- [67] T. Ono and K. Hirose, *Phys. Rev. Lett.* **82**, 5016 (1999).
- [68] P. Pulay, *Chem. Phys. Lett.* **73**, 393 (1980).
- [69] P. Pulay, *J. Comp. Chem.* **3**, 556 (1982).
- [70] D. R. Bowler and M. J. Gillan, *Chem. Phys. Lett.* **325**, 473 (2000).
- [71] G. P. Kerker, *Phys. Rev. B* **23**, 3082 (1981).
- [72] M. Manninen, R. M. Nieminen, P. Hautojärvi, and J. Arponen, *Phys. Rev. B* **12**, 4012 (1975).
- [73] J. Arponen, P. Hautojärvi, R. M. Nieminen, and E. Pajanne, *J. Phys. F* **3**, 2092 (1973).
- [74] R. M. Nieminen, *J. Phys. F* **7**, 375 (1977).
- [75] J. Auer and E. Krotscheck, *Comp. Phys. Comm.* **118**, 139 (1999).
- [76] J. Auer and E. Krotscheck, *Comp. Phys. Comm.* **151**, 139 (2003).
- [77] M. Aichinger and E. Krotscheck, submitted to *Comp. Phys. Comm.* (2004).
- [78] H. A. van der Vorst, *Iterative Krylov Methods for large linear systems* (Cambridge University Press).
- [79] T. Torsti. unpublished (1997); M. Heiskanen. unpublished (1998).
- [80] J. Dongarra, in *Templates for the solution of Algebraic Eigenvalue Problems: A Practical Guide*, edited by Z. Bai, J. Demmel, J. Dongarra, A. Ruhe, and H. van der Vorst (Philadelphia, 2000), 372.
- [81] J. Auer, E. Krotscheck, and S. A. Chin, *J. Chem. Phys.* **115**, 6841 (2001).
- [82] M. A. L. Marques, A. Castro, G. F. Bertsch, and A. Rubio, *Comp. Phys. Comm.* **151**, 60 (2003).
- [83] J. R. Chelikowsky, L. Kronik, and I. Vasiliev, *J. Phys. Cond. Matt.* **15**, R1517 (2003).
- [84] S. Riikonen, T. Torsti, M. J. Puska, and R. M. Nieminen, unpublished (2002).

- [85] J. P. Perdew, K. Burke, and M. Ernzerhof, *Phys. Rev. Lett* **77**, 3865 (1996).
- [86] J. A. White and D. M. Bird, *Phys. Rev. B* **50**, 4954 (1994).
- [87] For an overview, see L. Jacak, P. Hawrylak, and A. Wójs, *Quantum dots* (Springer, Berlin, 1998).
- [88] See, e.g., L. P. Kouwenhoven, D. G. Austing, and S. Tarucha, *Rep. Prog. Phys.* **64**, 701 (2001); S. M. Reimann and M. Manninen, *Rev. Mod. Phys.* **74**, 1283 (2002).
- [89] H. Saarikoski, E. Räsänen, S. Siljamäki, A. Harju, M. J. Puska, and R. M. Nieminen, *Phys. Rev. B* **67**, 205327 (2003).
- [90] C. Attacalite, S. Moroni, P. Gori-Giorgi, and G. B. Bachelet, *Phys. Rev. Lett.* **88**, 256601 (2002).
- [91] B. Tanatar and D. M. Ceperley, *Phys. Rev. B* **39**, 5005 (1989).
- [92] E. Räsänen, H. Saarikoski, M. J. Puska, and R. M. Nieminen, *Phys. Rev. B* **67**, 035326 (2003).
- [93] C. E. Creffield, W. Häusler, J. H. Jefferson, and S. Sarkar, *Phys. Rev. B* **59**, 10719 (1999).
- [94] E. Räsänen, H. Saarikoski, V. N. Stavrou, A. Harju, M. J. Puska, and R. M. Nieminen, *Phys. Rev. B* **67**, 235307 (2003).
- [95] D. G. Austing, S. Sasaki, S. Tarucha, S. M. Reimann, M. Koskinen, and M. Manninen, *Phys. Rev. B* **60**, 11514 (1999).
- [96] A. Harju, E. Räsänen, H. Saarikoski, M. J. Puska, R. M. Nieminen, and K. Niemelä, *Phys. Rev. B* **69**, 153101 (2004).
- [97] T. H. Oosterkamp, J. W. Janssen, L. P. Kouwenhoven, D. G. Austing, T. Honda, and S. Tarucha, *Phys. Rev. Lett.* **82**, 2931 (1999).
- [98] E. Räsänen, A. Harju, M. J. Puska, and R. M. Nieminen, *Phys. Rev. B* **69**, 165309 (2004).
- [99] S. M. Reimann, M. Koskinen, M. Manninen, and B. R. Mottelson, *Phys. Rev. Lett.* **83**, 3270 (1999).
- [100] H. Saarikoski, A. Harju, M. J. Puska, and R. M. Nieminen, *Phys. Rev. Lett.* **93**, 116802 (2004).
- [101] H. Saarikoski, S. M. Reimann, E. Räsänen, A. Harju, and M. J. Puska, submitted to *Phys. Rev. B*.
- [102] H. Saarikoski, A. Harju, M. J. Puska, and R. M. Nieminen, to appear in *Physica E*.
- [103] M. Toreblad, M. Borgh, M. Koskinen, M. Manninen, and S. M. Reimann, *Phys. Rev. Lett.* **93**, 090407 (2004).
- [104] E. Räsänen, J. Könemann, R. J. Haug, M. J. Puska, and R. M. Nieminen, *Phys. Rev. B* **70**, 115308 (2004).

- [105] P. Havu, T. Torsti, M. J. Puska, and R. M. Nieminen, *Phys. Rev. B* **66**, 075401 (2002).
- [106] T. Torsti, V. Lindberg, M. J. Puska, and B. Hellsing, *Phys. Rev. B* **66**, 235420 (2002).
- [107] E. Ogando, T. Torsti, M. J. Puska, and N. Zabala, *Phys. Rev. B* **67**, 075417 (2003).
- [108] M. Hakala, M. J. Puska, and R. M. Nieminen, *Phys. Rev. B* **57**, 7621 (1998).
- [109] K. Saarinen and V. Ranki, *J. Phys.: Condens. Matter* **15**, S2791 (2003).
- [110] K. Saarinen, J. Nissilä, H. Kauppinen, M. Hakala, M. J. Puska, P. Hautojärvi, and C. Corbel, *Phys. Rev. Lett.* **82**, 1883 (1999).
- [111] E. Boroński and R. M. Nieminen, *Phys. Rev. B* **34**, 3820 (1986).
- [112] M. Alatalo, B. Barbiellini, M. Hakala, H. Kauppinen, T. Korhonen, M. J. Puska, K. Saarinen, P. Hautojärvi, and R. M. Nieminen, *Phys. Rev. B* **54**, 2397 (1996).
- [113] G. Kresse and D. Joubert, *Phys. Rev. B* **59**, 1758 (1999).
- [114] I. Makkonen, M. Hakala, and M. J. Puska, to be published.